Deciphering cellular and molecular determinants of human DPCD protein in complex with RUVBL1/RUVBL2 AAA-ATPases

Raphael dos Santos Morais, Paulo E Santo, Marie Ley, Cédric Schelcher, Yoann Abel, Laura Plassart, Evolène Deslignière, Marie-Eve Chagot, Marc Quinternet, Ana C F Paiva, et al.

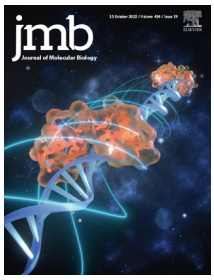

Deciphering cellular and molecular determinants of human DPCD protein in complex with RUVBL1/RUVBL2 AAA-ATPases

Raphael Dos Santos Morais [1†*], Paulo E. Santo [2,3†], Marie Ley [4,5†], Cédric Schelcher [1], Yoann Abel [6,7], Laura Plassart [8], Evolène Deslignière [4,5], Marie-Eve Chagot [1], Marc Quinternet [9], Ana C. F. Paiva [2,3], Steve Hessmann [4,5], Nelly Morellet [10], Pedro M. F. Sousa [2,3], Franck Vandermoere [11], Edouard Bertrand [6,7], Bruno Charpentier [1], Tiago M. Bandeiras [2,3], Célia Plisson-Chastang [8], Céline Verheggen [6,7], Sarah Cianférani [4,5*] and Xavier Manival [1*]

*1 - **IMoPA,** CNRS, Université de Lorraine, Nancy F-54000, France*
*2 - **iBET,** Instituto de Biologia Experimental e Tecnológica, Apartado 12, 2781-901 Oeiras, Portugal*
*3 - **Instituto de Tecnologia Química e Biológica António Xavier,** Universidade Nova de Lisboa, Av. da República, 2780-157 Oeiras, Portugal*
*4 - **Laboratoire de Spectrométrie de Masse BioOrganique,** Université de Strasbourg, CNRS, IPHC UMR 7178, Strasbourg 67000, France*
*5 - **Infrastructure Nationale de Protéomique ProFI – FR2048 CNRS,** 67087 Strasbourg, France*
*6 - **IGH,** CNRS, Univ Montpellier, Montpellier, France*
*7 - **Equipe labélisée Ligue Nationale Contre le Cancer,** 34293 Montpellier, France*
*8 - **MCD,** Centre de Biologie Intégrative (CBI), University of Toulouse, CNRS, UPS, 31062 Toulouse, France*
*9 - **Université de Lorraine,** CNRS, INSERM, IBSLor, Biophysics and Structural Biology Core Facility, F-54000, France*
*10 - **Très Grandes Infrastructures de Recherche,** Institut de Chimie des Substances Naturelles – CNRS, 1 avenue de la Terrasse, 91190 Gif-sur-Yvette, France*
*11 - **IGF,** CNRS, INSERM, Univ Montpellier, Montpellier, France*

Correspondence to Raphael Dos Santos Morais, Sarah Cianférani and Xavier Manival:
https://doi.org/10.1016/j.jmb.2022.167760
Edited by J. Buchner

Abstract

DPCD is a protein that may play a role in cilia formation and whose absence leads to primary ciliary dyskinesia (PCD), a rare disease caused by impairment of ciliated cells. Except for high-throughput studies that identified DPCD as a possible RUVBL1 (R1) and RUVBL2 (R2) partner, no in-depth cellular, biochemical, and structural investigation involving DPCD have been reported so far. R1 and R2 proteins are ubiquitous highly conserved AAA + family ATPases that assemble and mature a plethora of macromolecular complexes and are pivotal in numerous cellular processes, especially by guaranteeing a co-chaperoning function within R2TP or R2TP-like machineries. In the present study, we identified DPCD as a new R1R2 partner *in vivo*. We show that DPCD interacts directly with R1 and R2 *in vitro* and in cells. We characterized the physico-chemical properties of DPCD in solution and built a 3D model of DPCD. In addition, we used a variety of orthogonal biophysical techniques including small-angle X-ray scattering, structural mass spectrometry and electron microscopy to assess the molecular determinants of DPCD interaction with R1R2. Interestingly, DPCD disrupts the dodecameric state of R1R2 complex upon binding and this interaction occurs mainly via the DII domains of R1R2.

Introduction

Primary Ciliary Dyskinesia (PCD) is a genetically heterogeneous autosomal recessive disorder caused by mutations and characterized by immotile, dysmotile, or absent cilia. Cilia are highly conserved microtubule-based organelles that can be divided into two major types: motile cilia and non-motile cilia. Non-motile cilia, also called primary cilia, serve as sensory organelles, while motile cilia serve as flagella. The dysfunction of motile cilia causes ciliopathies with many phenotypes, including neonatal respiratory distress, chronic pulmonary disease, female and male infertility, organ laterality defects, hydrocephalus, and congenital heart defects.[1] Motile cilia are complex ultrastructures composed of a hundred proteins including axonemal dyneins that form the outer- and inner-arms (ODA and IDA) along doublet microtubules.[2] These multicomponent microtubule motors provide the force for ciliary beating resulting from ATPase activity and are built around heavy chain (HC) motor units that associate with WD-repeat intermediate chain (ICs) and various light chains (LCs).[3] Since ribosomes are absent from cilia, all axonemal dynein must be synthesized in the cytoplasm of the cell body and then transported and delivered precisely to the ciliary end.[4] Mutations in PCD genes usually cause the absence of ODA and/or IDA associated with microtubular disorganization and/or central pair organization defects.[5] In mice, among these genes, Zariwala and collaborators identified *DPCD*, which stands for deleted in a mouse model of primary ciliary dyskinesia.[6–7] Northern blots on about 20 human tissues showed an abundance of DPCD mRNA but only in testis[7] while DPCD protein was identified in human sperm.[8] In culture of human bronchial epithelial cells that differentiate to form a heavily ciliated epithelium, DPCD expression increased over time like other cilia-specific genes.[7] Examination of a group of PCD patients with mutations in DCPD showed defects in the IDA and ODA but none of the sequence variants was confirmed as the direct cause of the disease.

DPCD is poorly described at the protein level. It comprises 203 amino acids (23 kDa), has no functional homologs, and its function and 3D structure are currently unknown. DPCD was found to associate with the RUVBL1 (R1, also called Pontin) and RUVBL2 (R2, also called Reptin) in proteomic studies in humans[9–12] and in mouse cells,[13] which is consistent with R1 being found essential in the pre-assembly of the ciliary protein complex.[13] In mouse models, DPCD was found to be associated with DNAAF1 (Dynein axonemal assembly factor 1) in a co-immunoprecipitation assay.[13] This strengthens the potential role of DPCD in dynein arm assembly and more generally in cilia formation.

Given the complexity of axonemal dynein motors, many factors are required for their stable assembly in cytoplasm and their transport to the axonemal super-structure.[14] Among these factors, R2TP, a multiprotein complex acting in concert with the HSP70 and HSP90 chaperones, enables the stability, maturation, and quaternary assembly of functional macromolecular complexes. R2TP was originally identified in yeast[15] and is involved in many different cellular pathways. R2TP includes R1 (Rvb1 in yeast) and R2 (Rvb2 in yeast), two highly conserved ATPases Associated with diverse cellular Activities (AAA+) that form a functional alternating heterohexamer, and RNA polymerase II-associated protein 3 (RPAP3, Tah1p in yeast) and PIH1 domain-containing protein 1 (PIH1D1, Pih1p in yeast) proteins constituting a heterodimer. RPAP3 is the adapter for HSP70/90, and PIH1D1 mediates client protein recruitment. The sequence of R1R2 encompasses three domains: the αβα domain I (DI) and the α-helical domain III (DIII) that form the alternating AAA ring (ATPase or AAA-face), while a central and protruding domain II (DII-face, at the opposite of the AAA-face) represents a specific insertion into the core AAA+ domains. The DII domain is subdivided into DII_{int} including an α-helical bundle and a long flexible antiparallel β stalk, and DII_{ext} structurally equivalent to an oligonucleotide/oligosaccharide-binding (OB)-fold, which is an ssDNA binding domain. The DII-face represents a scaffolding platform within the R1R2 hexamer to recruit the majority of their clients/cofactors.

In vivo, ATP binding or hydrolysis by R1 or R2 is essential for all their postponed activities. For example, R1R2 ATPase activity is required for the maturation and/or disassembly of the PAQosome complex.[16] To date, all analysis of the 3D structures of free R1R2 revealed that nucleotide, most frequently ADP, is present in the binding pocket of each AAA-subunit even if it was not added during purification.[17–19] The binding pocket requires for nucleotide hydrolysis the arginine finger motif provided by the adjacent subunit in the hexamer ring. The hexamerization of R1-ADP blocks the nucleotide binding pocket, thus rendering an exchange from ADP to ATP impossible.[19] This point partially explains the weak ATPase activity of recombinant purified proteins,[17] unless DII domains are truncated, most likely mimicking cofactor regulation. Recent crystal structures suggest communication between the DII and the outer faces of ATPase to regulate this exchange. The ordered N-terminus of the R2 subunit, comprising the His-(Ser)-His motif, interacts with both the nucleotide and DII, thereby preventing the nucleotide to be released from its pocket.[20] The cryo-EM structure of the human R2TP revealed its structural organization as well as the pivotal role of PIH1D1.[21–22] These authors proposed that the binding of one PIH1D1 molecule

to the DII of one R2 subunit disorders the N-terminal segment of R2 and releases the ADP nucleotide likely to promote ATP turnover. Similarly, the binding of DHX34 to R1R2 displaces the N-terminal region in each R2 subunit and leads to the loss of nucleotides, allowing DHX34 to down-regulate R2 ATPase activity.[23] Very recently, ZNHIT2, a specific adaptor of the U5 snRNP biogenesis, was shown to induce changes in N-terminal regions of RUVBL2 and nucleotides were lost in all R2 protomers.[24] However, this type of mechanism remains hypothetical, as other authors were unable to observe significant displacement of the nucleotide from its active site when R2TP formed.[25]

Recently, it was suggested that other multiprotein complexes, homologous to R2TP, could form in cells in a tissue-specific manner to interact with particular adaptors and protein clients[11,26]: (*i*) R2SP where RPAP3 and PIH1D1 are replaced by SPAG1 (Sperm-associated antigen 1) and PIH1D2 (PIH1 domain-containing protein 2) respectively forming the SP heterodimer, (*ii*) R2SD where RPAP3 and PIH1D1 are replaced by SPAG1 and DNAAF2 (Dynein axonemal assembly factor 2, also Kintoun), (*iii*) D2 with DYX1C1 (Dyslexia susceptibility 1 candidate gene 1 protein, also DNAAF4)-a (a isoform) and DNAAF2, and (*iv*) DP with DYX1C1-c (c isoform) and PIH1D3. In mammals, R2TP associates with a Prefoldin-like (PFDL) module to form the PAQosome (Particle for Arrangement of Quaternary structure), a 12-subunit chaperone complex.[27,28] The PFDL module forms a hexameric structure that contains two α subunits (UXT and URI1) and four β subunits (PFDN2, PFDN6, PDRG1, and ASDURF for ASNSD1 upstream open reading frame protein). The PAQosome also includes two additional components, the RNA Pol I/II/III shared subunit POLR2E, and the Tryptophan/Aspartate Repeat 92 (WDR92, also known as Monad).[27] WDR92 has been reported to associate with DPCD[9]. It is only expressed in organisms that encode axonemal dynein.[29] FlyAtlas 2 adult expression data show that *Drosophila Wdr92* is highly and specifically expressed in testis in developing spermatocytes and is confined to the cytoplasm.[30] Recent biochemical data on *Chlamydomonas* revealed that Wdr92 is required for the cytoplasmic stability of ODA HCs.[29] The R2TP subunit RPAP3/PIH1D1 associates with Wdr92 which, in turn, is associated with dynein chains and DNAAFs.[31] Moreover, the association of Wdr92 protein with Spag1 is facilitated by the presence of R1 and R2.[31] The loss of Wdr92 leads to the malfunction of dynein arm assembly into sperm flagella and sensory neuronal cilia. To summarize, the R2TP/R2SP/R2SD/PAQosome complexes are thought to regulate the correct architectural preassembly of ciliary dynein motor, and malfunction of any of these key steps leads to PCD. In *Drosophila,* Wdr92 is hypothesized to be a new dedicated DNAAF.

In the present study, we identified *in vivo* DPCD partners, unveiled the first cellular, biochemical, and structural informations concerning human DPCD using fluorescence microscopy, SILAC- and LUMIER-IPs, and a series of structural biology techniques among which SAXS, NMR and structural mass spectrometry (structural MS). We first built a 3D model of the free DPCD structure based on experimental structural data. We next identified a direct sub-micromolar affinity interaction between up to 3 DPCD and one hexameric R1R2 (R1R2D complex) thanks to native MS and ITC. Additional structural data on the R1R2D complex obtained by SEC-SAXS, negative staining electron microscopy and cross-linking MS (XL-MS) confirmed that the interaction of DPCD occurs on R1R2 hexamers and dissociates the R1R2 dodecameric assembly. Finally, we discuss the putative role and biological relevance of DPCD in R2TP, R2TP-like or R1R2-related complexes.

Material and methods

Cell culture and cell line construction

HeLa Flp-In cells were a gift from S. Emiliani (Institut Cochin, Paris). HEK-293 T cells were obtained from the ATCC collection. All cells were grown at 37 °C, 5% CO_2 and cDNA transfections were done with JetPrime (Ozyme). HeLa Flp-In and HEK-293 T cells were grown in Dulbecco's Modified Eagle Medium (DMEM) containing 10% fetal bovine serum (FBS), glutamine (2.9 mg/mL), and penicillin/streptomycin (10 U/mL). For SILAC, after plasmid recombination at the FRT (Flp Recombination Target) site of HeLa Flp-In by co-transfection of FlpO expression plasmid and $pcDNA_5$-GFP-DPCD, clones were selected in Hygromycin B (150 μg/mL), picked individually, and characterized by Western blot and fluorescence microscopy.

SILAC-IP and proteomic analysis

For the SILAC experiment, a HeLa Flp-In clone expressing GFP-DPCD was grown for 15 days in isotopically semi-heavy label media containing L-Lysine-^{2}HCl (^{2}H4, 96–98%) and L-Arginine-HCl (^{13}C6, 99%) (percentages represent the isotopic purity of the labeled amino acids, CIL/Eurisotop). The parental cell line that does not express GFP-DPCD was grown in light non-labeled media (R0K0, L). Eight 15-cm diameter plates were used per condition. Cells were rinsed with PBS, trypsinized and cryoground in liquid nitrogen, and the resulting powder was resuspended in HNT lysis buffer (20 mM HEPES, pH 7.4, 150 mM NaCl, 0.5% triton X-100, protease inhibitor cocktail (cOmplete, Roche). Extracts were incubated for 20 min at 4 °C and clarified by centrifugation for

10 min at 20,000 × *g*. Before immunoprecipitation, extracts were pre-cleared by incubation with Protein G Sepharose beads (GE healthcare) for 1 h at 4 °C. Each extract was then incubated with 50 μL of GFP-Trap beads (Chromotek) for 90 min at 4 °C, washed 5 times with HNT buffer, and the beads from the different isotopic conditions were pooled. Bound proteins were eluted by adding 1% SDS to the beads and boiling for 10 min. Proteomic analysis was performed as previously described.[11]

Lumier-IP

HEK-293 T cells were grown in 24-well plates and co-transfected with 450 ng of the RL fusion and 50 ng of the 3x FLAG-FL fusion using JetPrime transfection reagent (Ozyme). After 48 h, cells were extracted in 500 μL of ice-cold HNTG buffer (20 mM HEPES, pH 7.9, 150 mM NaCl, 1% Triton X-100, 10% glycerol, 1 mM $MgCl_2$, 1 mM EGTA) containing protease inhibitor cocktail (Roche), incubated for 15 min at 4 °C and spun down for 15 min at 4 °C at 20,000 × *g*. Aliquots (100 μL) of the extract were placed in two wells in a 96-well plate, one well-being coated with anti-FLAG antibody (10 μg/mL in 1X PBS, F1804 Sigma-Aldrich), and one control well with no antibodies. The plates were incubated for 3 h at 4 °C, and then washed 5 times with 300 μL of ice-cold HNTG for 10 min at 4 °C for each wash. After the last wash, 10 μL of 1X PLB (Promega) was added in each well. To measure the input, 2 μL of extract and 8 μL of 1X PLB were mixed in new wells. The plates were then incubated for 5 min at room temperature, and FL and RL luciferase activities were measured in IP and input wells using the dual luciferase kit (Promega). Co-IP efficiency was defined as the RL/FL ratio in the pellet, divided by the RL/FL ratio in the input. Unless otherwise stated, statistical significance was evaluated using a Z-test to test if co-IP efficiency in the anti-FLAG IP was more than 11 times higher than the mean values obtained in the control IP, i.e. with no antibodies.[11] In assays where the CB6644 drug was used,[32] the drug was added at a final concentration of 0.5 mM in the culture medium 4 h after transfection and left to stand for 48 h. The control, with no drug, was with DiMethyl SulfOxide (DMSO).

Protein expression and purification

Recombinant His-DPCD protein (Uniprot: Q9BVM2, 203 residues, optimized synthetic gene encoding the L156S natural variant, Life technologies) was overexpressed in the *E. coli* BL21(DE3) pRARE2 strain using a pnEA-3CH vector.[33]

Bacteria were transformed with the corresponding plasmid and a clone was selected on LB agar medium with ampicillin. Bacteria were grown in LB medium at 37 °C and when the OD of 600 nm reached ∼ 0.7–1, protein production was induced with 0.2 mM IsoPropyl β-D-1-ThioGalactopyranoside (IPTG). Bacterial cultures were incubated overnight at 20 °C in a New Brunswick (Innova®) 44R Shaker at 180 rpm, and then harvested by centrifugation at 4,500 × *g*. Bacterial cells were broken down by sonication in lysis buffer (25 mM HEPES pH 7.5, 300 mM NaCl, 5% glycerol, 1 mM TCEP, 10 mM imidazole). The suspension was supplemented with 5 U/mL of DENARASE® (c-LEcta) and centrifuged to pellet cellular debris (30 min, 4 °C, 45,000 × *g*). The supernatant was filtered at 0.22 μm and injected onto a HiTrap TALON (Cytiva). The 5 mL prepacked column was washed extensively with lysis buffer (without TCEP), and then proteins were eluted in the same buffer but containing 300 mM imidazole. The His-tag was removed by Human RhinoVirus 3C (HRV-3C, Cytiva) cleavage overnight, unless otherwise stated. DPCD was finally polished in a final size exclusion chromatography step using Superdex 75 or 200 columns (16/60, Cytiva) equilibrated in HNGT buffer (20 mM HEPES, 150 mM NaCl, 1% glycerol, 1 mM TCEP). Protein purity was assessed by SDS-PAGE stained with Coomassie blue and the concentration was determined spectrophotometrically using a molar extinction coefficient of 32 430 $M^{-1}.cm^{-1}$. For the SEC-SLS of DPCD alone and circular dichroism (CD) experiments, the 6xHis tag was exceptionally preserved.

Recombinant R1R2 proteins (Uniprot: Q9Y265 and Q9Y230) were purified as described in[11] with the following modifications. R2 has a C-terminal FLAG_FH8 Tag preceded by HRV-3C protease cleavage site. Peak fractions collected from the HisTrap were incubated with 5 mM $CaCl_2$ for 1 h and loaded onto an HiPrep Octyl FF 16/10 column (Cytiva) equilibrated in Buffer B (20 mM HEPES pH 8.0, 200 mM NaCl, 5 mM $CaCl_2$, 0.5 mM TCEP). Bound proteins were eluted using Buffer C (Buffer B without NaCl, $CaCl_2$, and supplemented with 5 mM EDTA). The FLAG-FH8 tag in the collected samples was removed by incubation for 18 h at 4 °C with 1% (w/w) HRV-3C protease (Thermo Fisher Scientific). A Superose 6 column equilibrated with Buffer D (20 mM HEPES pH 8.0, 150 mM NaCl, 0.5 mM TCEP) was used to allow the isolation of the main oligomeric species. The peak fractions were pooled and concentrated to 17.3 mg/mL using a 30 kDa Cut-off Amicon Ultra centrifugal filter (Millipore). R1ΔDIIR2ΔDII and R1_D302NR2_D299N purifications were performed as described above except that all buffers were supplemented with ATP in the latter purifica-

tion. All purification steps were carried out at room temperature and were monitored by NuPage Bis-Tris gels (Invitrogen, NP0302).

Far-UV circular dichroism analysis

The Far-UV circular dichroism spectrum of His-DPCD was recorded on a Chirascan spectropolarimeter (Applied Photophysics) from 190 to 260 nm in 0.01 cm pathlength Hellma cells. Blanks corresponding to the buffer were subtracted from the respective spectra. His-DPCD was analyzed at 50 μM and units are expressed as Molar Residue Ellipticity (MRE, in degrees.cm^2.dmol^{-1}.residue^{-1}). The measurement temperature was 20 °C. The secondary structure content was estimated using the BeStSel server (http://bestsel.elte.hu/index.php).[34–35]

Size exclusion chromatography coupled with static light scattering (SEC-SLS)

SEC-SLS experiments were performed at 30 °C with an AKTA Explorer HPLC system (Cytiva) coupled to light scattering and refractive index detectors (Viscotek TDA302, Malvern Panalytical). The SEC columns (Shodex KW803 or KW804, 7 μm, 8 mm ID × 300 mm, void volume ∼ 6 mL, total volume ∼ 12.5 mL or Agilent BioSEC5-500 Å, 4.6 mm ID × 300 mm, void volume ∼ 2 mL, total volume ∼ 5 mL) were equilibrated either with PBS (pH 7.4, Gibco, Thermo Fisher Scientific) or HNGT buffer (5 mM TCEP). The flow rate ranged from 0.2 to 0.5 mL/min. Data were processed with OmniSEC software (v5.12, Malvern Panalytical) using RALS/LALS detectors. The refractometer was used to determine the protein concentration and the refractive index increment value (dn/dc) used to determine the molecular weight (MW) was 0.185 mL/g. Hydrodynamic radii were estimated with SEC protein standards (BEH200, Waters).

Nuclear magnetic resonance (NMR)

^{13}C/^{15}N and ^{2}H/^{13}C/^{15}N samples of DPCD were prepared as described above, except those bacteria were grown in aqueous or deuterated minimal M9 media supplemented with $^{15}NH_4Cl$ and ^{13}C-d6-Glucose as sole nutrient source. The recombinant proteins were purified as described above, the final buffer being 10 mM NaPi, pH 6.5, 300 mM NaCl, 5 mM DTT deuterated. ^{1}H-^{15}N TROSY-HSQC, ^{1}H-^{15}N NOESY-HSQC and triple resonance HNCA/trHNCA, HNCO, HNCACB/trHNCACB and CBCACONH/trCBCACONH spectra were recorded at 298 K on 600 MHz and 950 MHz spectrometers equipped with cryoprobes. Data were processed with TopSpin-3.0 (Bruker) and analyzed with CARA.[36] Assigned HN, N, CO, Cα and Cβ chemical shifts were derived into secondary structures using TALOS-N.[37]

Isothermal titration calorimetry (ITC)

Protein/protein interactions were characterized at 30 °C using a microcalorimeter (MicroCal iTC200, Malvern Panalytical) in HNGT buffer. DPCD was placed into the syringe at a concentration of 203 μM and 6 μM of R1/R2 hexamers were injected into the cell. Nineteen successive 2 μL injections were performed, except for the first injection which was only 0.5 μL to prime the syringe. The rotation of the blade was set to 300 rpm. Data were processed with NITPIC[38] (v1.2.7) and NanoAnalyze (v3.10.0, TA instruments) software to determine the dissociation constant (K_d), the stoichiometry (n), and the thermodynamic parameters: enthalpy (ΔH), entropy (ΔS) and free energy (ΔG).

Chromatographic co-elution assay

For the formation of R1R2D complex, 1.93 nmol DPCD (23.2 kDa) were combined with different ratios of R1R2 and incubated for 18 h at 4 °C. Buffer D was added to reach a final volume of 200 μL immediately before injection in Superose 6 10/30 GL Increase (Cytiva). A 100-μL loop was used with a flow rate of 0.75 mL/min using an AKTA purifier system (Cytiva). The eluting protein was detected by UV absorbance at 280 nm. This elution profile was compared to injections of 1.93 nmol R1/R2 and DPCD alone. All chromatographic steps were carried out at room temperature and were monitored by NuPage Bis-Tris gels (Invitrogen, NP0302). Protein molecular masses were estimated by comparison with six molecular mass standards (Sigma, St. Louis, MI, USA): Thyroglobulin (669 kDa), Apoferritin (443 kDa), β-Amylase (200 kDa), Alcohol Dehydrogenase (150 kDa), Bovine Serum Albumin (66 kDa), and Cytochrome C (12.4 kDa).

Native mass spectrometry (MS) and ion mobility (IM-MS) measurements

For native MS analysis, samples were buffer exchanged against ammonium acetate (150 mM, pH 7.5, Sigma, St. Louis, MO, USA), using Zeba Spin desalting columns (Thermo Fisher Scientific, Rockford, IL, USA). Sample concentrations were determined by UV absorbance using a NanoDrop 2000 spectrophotometer (Thermo Fisher Scientific, France). Native MS analyses were carried out on an Orbitrap Exactive Plus EMR (Thermo Fisher Scientific, Bremen, Germany) coupled to an automated chip-based nanoelectrospray source (TriVersa NanoMate, Advion Biosciences, Ithaca, U.S.A.) operating in positive ion mode. The in-source collision-induced dissociation (CID) was set to 50 eV. The higher-energy collisional dissociation (HCD) cell was set to 200 eV for each analysis to improve the desolvation. The trapping gas pressure was set to

7 a.u. (corresponding to an ultra-high vacuum of 1.10^{-9} mbar). To improve the transmission of the high MW species, the voltages on the injection-, inter-, and bent-flatapoles were set to 2 V. Acquisitions were performed in the *m/z* range 1,000–20,000 with a 3 s scan time and a resolution of 8,750 at 200 *m/z* with an automatic gain control (AGC) target set to 1.10^6 and a maximum injection time set to 100 ms. External calibration was performed using singly charged ions produced by a 2 g/L solution of cesium iodide in 2-propanol/water (50/50 v/v). Orbitrap MS data were interpreted using BioPharmaFinder v3.2 (Thermo Fisher Scientific, Bremen, Germany).

Native IM-MS experiments were performed on a hybrid quadrupole/travelling wave ion mobility spectrometry (TWIMS)/time-of-flight mass spectrometer (Synapt G2 HDMS, Waters, Wilmslow, UK). The Synapt was operated in positive ionization mode. Parameters – sample cone 5 V, trap gas 5 mL/min (argon) and backing pressure 6 mbar – were optimized to preserve noncovalent interactions and to minimize ion activation. For DPCD, ions were focused in the helium cell (150 mL/min), prior to separation in the IM cell with a nitrogen flow rate of 25 mL/min. The wave velocity (WV) and height (WH) were set to 1,250 m/s and 40 V, respectively. For R1R2 and R1R2D complexes, gas flow rates of 120 mL/min (He) and 60 mL/min (N_2) were used, and WH and WV parameters were fixed to 550 m/s and 40 V, respectively. IM-MS experiments were recorded in triplicate under identical instrumental conditions. Arrival time distributions (ATD) were extracted with MassLynx v4.1 (Waters, Manchester, UK). ATDs were converted into collision cross sections ($^{TW}CCS_{N2}$) using alcohol dehydrogenase, pyruvate kinase and glutamate dehydrogenase as external calibrants, as reported elsewhere.[39–40] Experimental $^{TW}CCS_{N2}$ values were then compared with theoretical CCS using PDB files with the IMoS v1.10 software.[41] Nitrogen was considered as the drift gas, with a corresponding Van der Waals radius of 1.5 Å and gas polarizability of 1.7 Å^3. Calculations were performed using the projection approximation (PA) and the exact hard sphere scattering (EHSS) methods. Averaged theoretical CCS values were obtained from six independent calculations. For straightforward comparison of IM-MS results with solution-based techniques, IM radii ($R_{IM\text{-}MS}$) were derived from their corresponding $^{TW}CCS_{N2}$ assuming a spherical shape of the protein, with $R_{IM\text{-}MS} = (^{TW}CCS_{N2}/\pi)^{½}$.[42]

Differential scanning fluorimetry (DSF)

DSF was performed in MicroAmp EnduraPlate Optical 96-Well Clear Reaction Plates with Barcode (Applied Biosystems, Life Technologies, California, USA) using a QuantStudio 7 Flex Real-Time PCR System (Applied Biosystems). Protein samples were briefly centrifuged before preparation for the assay. The final reaction mixture (total volume 20 μL) contained either DPCD, R1R2, or R1R2D, and 4-fold Protein Thermal Shift Dye (Applied Biosystems) diluted in Buffer D. Melting curve data were recorded from 25 °C to 90 °C at an increment rate of 0.016 C. s^{-1}. Excitation and emissions filters were applied for Protein Thermal Shift Dye (470 nm and 520 nm, respectively) and for ROX reference dye (580 nm and 623 nm, respectively). The melting temperatures were obtained by calculating the midpoint of each transition, using Protein Thermal Shift Software™ v1.3. All the samples were tested in duplicate.

Dynamic light scattering (DLS) Analysis

A SpectroLight 610 (XtalConcepts GmbH, Hamburg, Germany) was used to perform serial DLS measurements. All the samples were centrifuged (15–30 min, 4 °C, 17,200 × *g*) in a benchtop centrifuge before measurement and were pipetted (each sample in duplicate, 1 μL per well) onto a 96 well Vapor Batch Plate (Jena Bioscience). Prior to use, the plates were filled with paraffin oil (Cat N. 18512, Merck) to protect the sample solutions from drying out. The laser wavelength was 660 nm at a power of 100 mW. The scattering angle for placement of the detector was set to 142°. All tested samples were kept in HEPES buffer so the refractive index (1.34) and viscosity (1.006 cP) of water were used for calculations. All the samples were measured at a constant temperature of 20 °C, one scan per drop with 20 measurements of 20 seconds each. R1/R2 and R1R2D were tested at a concentration of 1 mg/mL.

Small-angle X-ray scattering (SAXS) experiments and de novo protein prediction

SAXS data were obtained using SEC-SAXS on the SWING beam line at the French SOLEIL synchrotron (Saint-Aubin, France). Data were collected using an Eiger 4 M detector at a sample-detector distance of 2 m and at a wavelength of λ = 1.033 Å (*I(Q)* vs *Q*, where $Q = 4\pi\sin\theta/\lambda$, and 2θ is the scattering angle), covering a Q-range of 0.005–0.5 Å^{-1}. SEC-SAXS was performed at 15 °C with a Bio SEC5-500 Å HPLC column (4.6 mm ID × 300 mm, void volume ∼ 2 mL, total volume ∼ 5 mL, Agilent) equilibrated in HNGT buffer (5 mM TCEP) at 0.3 mL/min. Fifty microliters of samples at 5–12 mg/mL were injected into the column. The data were collected through the SEC peak of the protein as a series of 1-s exposures. Data reduction to absolute unit, frame averaging, and subtraction were performed with FOXTROT. Curves displaying a constant *Rg*, in a *Rg* versus frame number plot, were averaged and used for further characterization. Data were analyzed with the ATSAS suite[43] following the man-

ufacturer's guidelines unless indicated otherwise. The MW was determined using the volume of correlation method.[44] Ten *ab initio* models were generated with GASBOR software, the models were aligned and averaged with DAMAVER software. The models shown are those with the lowest χ^2 value. For DPCD, Tr-Rosetta[45] was used to predict *de novo* models. RoseTTAFold[46] and AlphaFold2[47] were also employed. The generated models were compared to SAXS data with CRYSOL. The model with the lowest χ^2 value was selected for further processing and was subjected to normal mode analysis using SREFLEX[48] through the ATSAS online interface (www.embl-hamburg.de/biosaxs/atsas-online). Data have been deposited in the SASBDB[49]: DPCD (SASDFF5), and R1R2D complex (SASDFH5).

Negative staining electron microscopy

R1R2 or DPCD-containing complexes were formed and purified as described above. Aliquots (3.5 μL) of the complexes (concentration: 20 μg/mL) were deposited on glow-discharged, 300 Mesh Copper carbon-coated grids (Quantifoil, Germany). After 1 min of incubation at room temperature, excess liquid was blotted, and the grids were stained with two successive drops of 1% uranyl acetate (3.5 μL was used for each blot). The first drop was immediately blotted, the second was left for ∼ 20 s on the grids before blotting. Finally, the grids were air-dried before observation on the electron microscopes of the METI platform (*Centre de Biologie Intégrative*, Toulouse, France). Initial images were recorded on a Jeol JEM-1400-HC operating at 80 kV and equipped with a Gatan Orius SC1000B CCD camera and DigitalMicrograph (Gatan, Inc.), at a magnification corresponding to a calibrated pixel size of 2.39 Å. For 2D classification, images were recorded on a JEOL JEM-2100 electron microscope (LaB6 cathode, operating voltage: 200 kV) with a Gatan US1000 CCD camera and DigitalMicrograph (Gatan, Inc.). Defoci ranged between −0.5 and −1.6 μm, and the calibrated pixel size corresponded to 2.35 Å. Single particle analysis (CTF estimation, particle picking and extraction, 2D classification) was performed using Relion 3.1.[50] For R1R2 complexes, 250 micrographs were recorded corresponding to 42,860 extracted particles that were further classified into 150 2D classes. For R1R2D complexes, 300 micrographs were recorded that yielded 59,629 extracted particles, subsequently classified into 250 2D classes. For R1R2 ΔDII, 300 micrographs were acquired from which 33,028 particles were extracted and classified into 150 2D classes.

Cross-linking MS (XL-MS)

Cross-linking reactions were conducted with 1.75 mg/mL protein solution. Freshly prepared 10 mM stock solution of disuccinimidyl dibutyric urea (DSBU, which reacts specifically with Lys residues) was added 100-fold molar excess. The reaction lasted 45 min at room temperature. The reaction was quenched for 20 min using NH_4HCO_3 to reach a final concentration of 20 mM. Disulfide was reduced by incubating the cross-linked complex solution with 5 mM DTT for 30 min at 37 °C. Alkylation was performed with 15 mM iodoacetamide (IAA) for 60 min in the dark. Trypsin/Lys-C mix (Promega, Madison, USA) was then added to reach a 1:50 enzyme: substrate ratio. Samples were incubated overnight at 37 °C. Digestion was quenched with 1% TFA. Peptides were cleaned up using SPE cartridges and samples were concentrated in a SpeedVac concentrator before LC/MS/MS analysis. NanoLC-MS/MS analysis was performed using a nanoAcquity Ultra-Performance-LC (Waters, Milford, USA) coupled to the Q-Exactive Plus Orbitrap mass spectrometer (Thermo Fisher Scientific, Bremen, Germany) with a nanoSpray source. Samples were trapped on a nanoACQUITY UPLC precolumn (C18, 180 μm × 20 mm, 5 μm particle size), and the peptides were separated on a nanoACQUITY UPLC column (C18, 75 μm × 250 mm with 1.7 μm particle size, Waters, Milford, USA) maintained at 60 °C. Mobile phase A was 0.1% (v/v) formic acid in water, and mobile phase B was 0.1% (v/v) formic acid in acetonitrile. The sample were first injected with a 105 min gradient (1–3 % B for 2 min, 3–35% B for 77 min, 35–90% B for 1 min, 90% B for 5 min, 90–1% B for 2 min and maintained 1% B for 2 min) at a flow rate of 400 nL/min. The Q Exactive Plus Orbitrap source temperature was set to 250 °C and the spray voltage to 1.8 kV. Full scan MS spectra (300–1,800 m/z) were acquired in positive mode at a resolution of 140,000, a maximum injection time of 50 ms and an AGC target value of 3.106 charges, with the lock-mass option enabled (polysiloxane ion from ambient air at 445.12 m/z). The 10 most intense multiple charged peptides per full scan (charge states > 2) were isolated using a 2 m/z window and fragmented using HCD (30 normalized collision energy, ± 3%). MS/MS spectra were acquired with a resolution of 35,000, a maximum injection time of 100 ms, an AGC target value of 1.105, and dynamic exclusion set to 60 s. The system was fully controlled by XCalibur software v3.0.63, 2013 (Thermo Scientific) and a NanoACQUITY UPLC console v1.51.3347 (Waters). Raw data collected were processed and converted into.mgf format. The MS/MS data were analyzed using MeroX software v2.0.1.4 (Götze et al., 2015). Mass tolerances of 5 ppm for precursor ions and of 10 ppm for product ions were applied. A 5% FDR cut-off and a signal-to-noise ≥ 2 were applied. Lys and Arg residues were considered as protease sites with a

maximum of three missed cleavages. Carbamidomethylation of cysteine was set as static modification and oxidation of methionine as variable modification (max. mod. 2). Primary amino groups (Lys side chains and N-termini) as well as primary hydroxyl groups (Ser, Thr and Tyr side chains) were considered as cross-linking sites. The cRap database was used in combination with the reporter ion scan event (RISEUP) mode with a maximum missing ion of 1. Cross-links composed of consecutive amino acid sequences were ignored. Each cross-linked product automatically annotated with MeroX was manually validated. Three different experiments were performed, and cross-linked peptides were validated when seen in 2 out of 3 experiments. The XL-MS data set has been deposited to the ProteomeXchange Consortium via the PRIDE[51] partner repository with the dataset identifier PXD031339.

Results

In vivo characterization of several complexes with DPCD

DPCD was first identified in association with R2TP or R2TP/PFDL in several high throughput studies.[9–10,13] To identify new DPCD key partners in a cellular environment, we first generated a 3xFLAG-GFP-DPCD fusion protein for cellular localization and quantitative proteomics.

Using fluorescence microscopy in HeLa cells, DPCD was found to be distributed throughout the cell in both the cytosol and the nucleoplasm (Figure 1(A)). Next, we created a HeLa Flip-In clone that stably expressed the fusion protein and performed quantitative proteomics using SILAC followed by immunoprecipitation (SILAC-IP). Proteomic analysis of anti-GFP IP obtained from this clone revealed two levels of protein enrichment (Figure 1(B)). At the first level, we found R1 and R2, which showed major enrichment in DPCD (SILAC ratio) and high intensity MS detection (comparable to the bait, Table S1),[62] suggesting a strong association between DPCD and R1R2. Interestingly, this is the first evidence to the existence of a unique R1R2D complex *in vivo*. The second level corresponds to proteins with milder but still significant (Bsignificance < 0.05) enrichment in DPCD and milder MS intensity (Table S1), suggesting fewer expressed interacting proteins or more labile protein–protein interactions. This second class includes R2TP core proteins such as RPAP3 and PIH1D1, R2TP clients like the U5 snRNP protein EFTUD2 and the U4, U6, U5 tri-snRNP protein AAR2, co-factors like ZNHIT2 and C2orf44/WDCP/MMAP, and core proteins of PAQosome like WDR92/Monad and POLR2E.[9,11,27] In this group, we also found HSP90/70 chaperones and their co-chaperones such as STIP1. We therefore conclude that DPCD associates with R2TP-HSP70/90-PAQosome complexes.

To confirm the interactions between DPCD and R2TP and some co-factors, we performed LUMIER-IP experiments, i.e. a quantitative immunoprecipitation assay that uses pairs of over-expressed proteins.[52] In these experiments, DPCD had a low percentage of CoIP with RPAP3, RPAP3-Cter and PIH1D1 (Figure 1(C)) and did not interact with WDR92 (Figure 1(D)). Conversely, RPAP3 N-terminal domain and PIH1D1 show in our assay with WDR92, high and intermediate signals, respectively, suggesting a strong interaction (Figure 1(D)). Surprisingly, full-size RPAP3 did not interact at all with WDR92. As signals for DPCD interactions with R1 WT and R2 WT were respectively, high and intermediate (Figure 1(E)), indirect association could explain the presence of RPAP3, PIH1D1 and WDR92 in the SILAC-IP of GFP-DPCD (Figure 1(B)).

We also investigated the interactions between DPCD and point functional mutants of R1 and R2 (Figure 1(E)). Concerning R1 mutants, DPCD still interacted with R357E (deletion of the trans-arginine finger) whereas *in vivo* binding with E303Q was lost (no ATP hydrolysis) and was reduced with K76M (no ATP binding). Concerning R2 mutants, the interaction was also reduced with E300Q (no ATP hydrolysis), K83M (no ATP binding), and R353E (deletion of the trans-arginine finger) compared to R2 WT. Moreover, we tested the effect of a selective (non-ATP-competitive) R1R2 ATPase inhibitor, the CB6644 drug, known to stabilize the ATP-bound state, on the interaction between DPCD and each individual RUVBL, in transfected cells.[32] This treatment eliminated the interaction between DPCD and R1 and R2 (Figure 1(F)). These data suggest that the interaction between DPCD and R1 and R2 relies on ATPase activity-dependent events that might be linked to subtle DII conformational changes during the ATPase cycle.

Biochemical and 3D structural characterization of DPCD in solution

At the protein level, DPCD is rarely described in the literature and almost no structural information is available, prompting us to characterize this protein in solution. The L156S natural variant (Uniprot: Q9BVM2) of DPCD (further referred as DPCD or D) was obtained with a high degree of purity (> 95%), assessed by SDS-PAGE with a band at ~ 25 kDa in line with the theoretical amino acid sequence and MS analysis (23,503.9 ± 1.0 Da) (Figure S1(A)). The calculated hydrodynamic radius was 24 Å (Table S2) and the oligomeric state of His-DPCD was determined using SEC-SLS with a molecular weight (MW) of ~ 30 kDa at the top of the peak, attesting that His-DPCD is monomeric in solution with HNGT buffer (Figure S1(B)). This was further confirmed

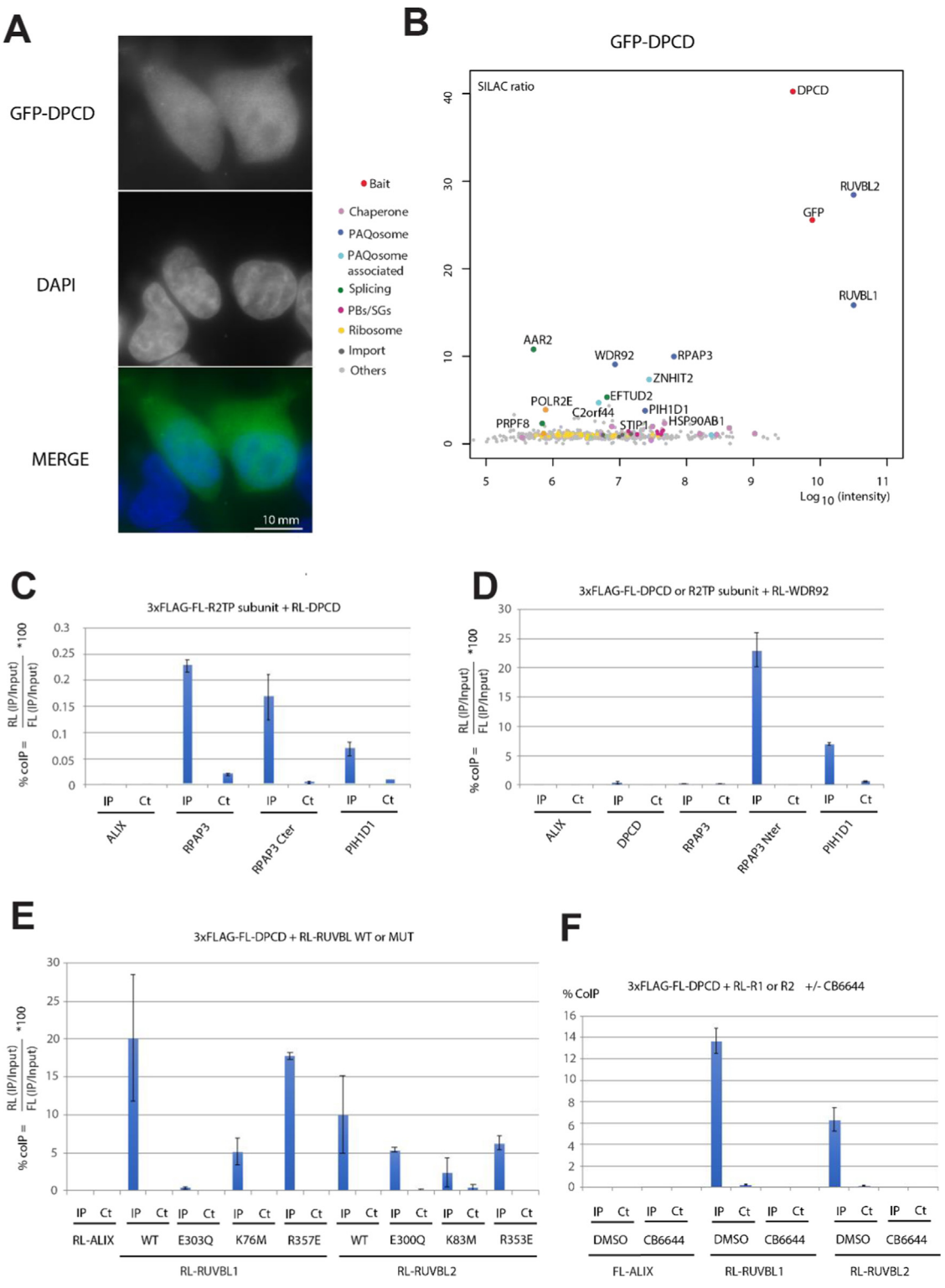

by native MS analysis, which also attested to the monomeric state of DPCD (Figure S1(C)). It is worth noting that DPCD tended to dimerize if the buffer was not supplemented with a reducing agent, meaning that oligomerization occurs through an inter-molecular disulfide bond. Supplementing the buffer with TCEP prevented the formation of multimeric forms (Figure S1(C)).

To assess the structural determinants of DPCD, the secondary structure was predicted using PSIPRED[53] (Figure S2(A)). Analysis estimated ~ 35% β-sheet and 15% α-helix, while the

remaining 50% amino acids are likely organized in a coil. Circular dichroism was used to confirm these *in silico* results experimentally and revealed that His-DPCD has the same secondary structure (Figure S2(B)). Although folded, half DPCD is composed of random coil structures.

Indeed, apart from the prediction of the CHORD-containing proteins and SGT1 (CS) domain in the C-terminal, no experimental 3D structural data are available concerning full-length DPCD either free or bound to potential protein partners. Despite several attempts using X-ray crystallography (XRC) at high resolution, we failed to obtain structural information concerning the free form. We then moved to solution-state NMR spectroscopy with $^{13}C/^{15}N$ and $^{2}H/^{13}C/^{15}N$ labeled samples of DPCD and a set of 2D and 3D spectra recorded at 600 and 950 MHz. First, the ^{1}H-^{15}N TROSY-HSQC spectrum displayed the features of a folded monomeric protein, in agreement with SEC-SLS and native MS analyses (Figure S2(C)). Unfortunately, in-depth analysis of the 3D spectra revealed missing backbone resonances at various spots in the protein, preventing complete and trustworthy assignment of DPCD resonances. Changes in temperature or in the concentration of the sample did not modify its dynamic behavior. This phenomenon was likely due to unfavorable exchange regimes between several fragments of the protein. Nevertheless, around 75% of the H_N, N, C_O, C_α and C_β nuclei in the protein were successfully assigned. Even if it was not possible to transform these partial NMR data into an accurate 3D structure, the values of the chemical shifts obtained for some of the residues were derived into secondary structures using the TALOS-N software (Figure S2(A)).[37] The predicted (PSIPRED, upper) and experimental (NMR, lower) patterns of secondary structures are in good agreement, confirming the global folded structure of the protein. Respectively, 13%, 37% and 50% of the assigned residues were folded in a helix, sheet, and coil, in agreement with the CD data. Interestingly, the NMR data support the presence of a CS domain ranging from residue K99 to residue K172 (Figure S2(C)). Note that the long unstructured regions in DPCD may impair protein crystallization.

To circumvent these difficulties, we changed to low-resolution SEC-SAXS experiments (Figure S3) to obtain structural insights and molecular clues about DPCD conformation in solution (Figure 2 and Tables S2 and S3). First, using the Guinier approximation, a radius of gyration (R_g) value of $\sim$ 22 Å was obtained. This value is in good agreement with the $R_{IM\text{-}MS}$ value of $\sim$ 27 Å (monomeric DPCD, charge state 9 +) derived from $^{TW}CCS_{N2}$ measurements obtained by IM-MS (Table S2). P(r) analysis (Figure 2(A), inset) showed a peak around 25 Å and a decrease to a D_{max} value of $\sim$ 78 Å. Dimensionless Kratky plots and Porod-Debye plots are typical of a protein with both folded and unfolded, or asymmetrical domains, but with preserved compactness (Figures S3(B) and S3 (C)). To shed light on DPCD 3D organization, *ab initio* low-resolution models were generated (Figure S3(D)). The *ab initio* models consisted of a disk-like shaped domain with an extended tail, in line with the P(r) analysis. To go further in the 3D characterization of DPCD, *de novo* models were generated with the trRosetta algorithm[45] (Figures 2 (B) and S3(E)), leading to four models with good scores (0.78). All the secondary structures predicted by the models are in line with PSIPRED prediction and TALOS-N determination (Figure S2(A)). In these models, a CS domain (K99-K172) is preceded by an additional domain of 5 antiparallel strands (Q14-Q66) (Figures 2(B) and S3(E)). Finally, the two α helices found in the N-term and C-term parts in the DPCD sequence are predicted to be close in space. To validate the accuracy and the reliability of these *de novo* models,[45] they were compared with SAXS experimental data (Figure 2 (A)). The theoretical SAXS curves of 4 of the models fit the experimental data remarkably well with equivalent χ^2 (5.5–6.5) whereas the fifth, which differs in the position of an unstructured loop, did not fit the data properly ($\chi^2 \sim 12.5$). Derived R_g values of $\sim$ 20 Å are in good agreement with the value of 22 Å determined experimentally. Of note, newly

Figure 1. *In vivo* characterization of the interaction between DPCD and RUVBL1/2. (A) Location of GFP-DPCD. Hela cells were transfected with plasmid coding for GFP-DPCD fusion. DAPI was used for DNA staining. (**B**) Proteomic analysis of GFP-DPCD partners by SILAC-IP. Graphs show SILAC ratios (y axis, specific versus control IP) as a function of signal abundance (x axis, $\log_{10}$(intensity)). Each dot represents a protein and is color coded according to the classification shown between panels A and B. The labeled dots highlight proteins that are relevant for this study. The full hit list with Significance B values is given in Table S1. (**C-F**) LUMIER-IP analysis of interactions. Graph plotting the % of co-IP efficiency for the interaction between co-expressed 3xFLAG-FL-R2TP subunits and RL-DPCD (**C**), 3xFLAG-FL-R2TP subunits or DPCD and RL-WDR92 (**D**), 3xFLAG-FL-DPCD and RL-R1 or R2 WT or mutant (**E**), 3xFLAG-FL-DPCD and RL-R1 or R2 with or without CB6644 treatment (**F**). The percentage of co-IP was calculated from the co-precipitated RL fusion protein (IP/Input ratios of RL activity), normalized with the IP/Input ratio of FL activity obtained in the anti-FLAG IP. The values are means of two or three experiments, each performed with duplicated values. ALIX was used as negative control. For each bait, Ct IP was done without antibody. Error bars represent standard deviations.

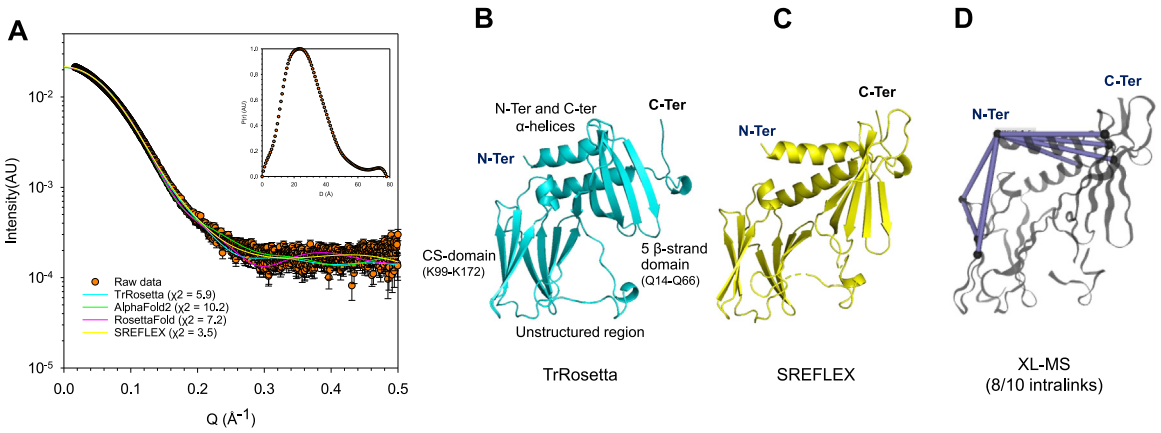

Figure 2. SEC-SAXS of DPCD. (**A**) Scattering intensity I(q) vs Q plot (orange dots). Lines correspond to Crysol fits of the models described in B (blue), C (yellow). The comparison with AlphaFold2 (green) and RoseTTAFold (pink) models are also displayed. Pair distribution function analysis is shown in the inset. (**B**) The trRosetta model of DPCD with the lowest χ^2 value. (**C**) DPCD trRosetta model after SAXS/NMA refinement. (**D**) Intralinks identified by XL-MS analysis and in line with the DPCD model.

developed methods, RoseTTAFold[46] and AlphaFold2[47] produced similar DPCD models, but with lower agreement to SAXS data (Figure 2(A)). Despite a good initial fit of SAXS data, the trRosetta model with the lowest χ^2 value was subjected to SAXS/NMA structural refinement to improve agreement with experimental data (Figure 2(C)). As expected, few domain shifts were observed with increased data fitting ($\chi^2 \sim 3.5–3.8$). We next used XL-MS with DSBU as chemical reagent to further validate the *in silico* DPCD 3D model. Interestingly, most of the intra-DPCD cross-links (8/10) were compatible considering Cα-Cα distances ranging from 6 to 30 Å (Figure 2(D), Table S4). Seven of these cross-links include the N-term part of DPCD, which is composed of residual residues from 3C protease cleavage (GPH) and turned out to be useful to validate the DPCD model, since Cα-Cα distances are fully compatible with the DPCD model. A reliable model based on *de novo* prediction and in line with experimental SAXS and XL-MS data is therefore proposed as a basis for further structural investigations.

Three DPCD molecules interact with R1R2 heterohexamer with sub-micromolar affinity

The formation of the R1R2-DPCD (R1R2D) complex was first analyzed using SEC-UV followed by SDS-PAGE analysis (Figure 3(A), top), which confirmed co-elution of DPCD, R1 and R2 with subsequent formation of a ternary complex. A shift of the SEC-UV elution peak towards lower hydrodynamic radii for the R1R2D complex compared to R1R2 alone was observed, suggesting a change in R1R2 oligomeric state from dodecamer to hexamer upon DPCD binding. To assess the specificity of the R1R2D interaction, similar SEC-UV analyses were conducted with R1R2 DII-truncated constructs (Figure 3(A), bottom). No co-elution was observed with R1R2 lacking DII domains, suggesting the interaction between R1R2 and DPCD mainly occurred through DII domains. The hydrodynamic radius of the R1R2D complex determined by SEC-UV using globular protein standards was smaller (73 Å) than that of R1R2 alone (94 Å). The same trend was confirmed by DLS in which the difference in the calculated hydrodynamic radius decreased from ∼ 70 to 63 Å for R1R2 and R1R2D, respectively, (Figure S4) in line with the proposed shift from dodecamer to hexamer in the R1R2 ring scaffold.

To evaluate the stoichiometry of the R1R2D complex through MW measurements, SEC-SLS experiments were performed and allowed a MW measurement of ∼ 370 kDa at the top of the peak, in agreement with one R1R2 hexamer interacting with three DPCD molecules (Figure 3(B)). To determine the R1R2D stoichiometry precisely, native MS experiments were performed and the binding of up to three DPCD molecules per R1R2 hexamer was validated (383,611 ± 66 Da, Figure 3(C)) again confirming that DPCD binding can change the R1R2 oligomeric state from dodecamer to hexamer (that coexist in absence of DPCD, Figure S5).

ITC (Figure 3(D)) enabled measurement of a dissociation constant (K_d) of ∼ 350 nM, attesting the high affinity between the protein partners. The calculated reaction stoichiometry (N-value) is ∼ 2.7 DPCD per 1 R1R2 hexamer, in agreement with native SEC-SLS and native MS data. The thermodynamic signature is characteristic of hydrogen bonding with unfavorable conformational modifications with negative values for ΔG and ΔH and a positive value for –TΔS (Figure 3(D), inset).

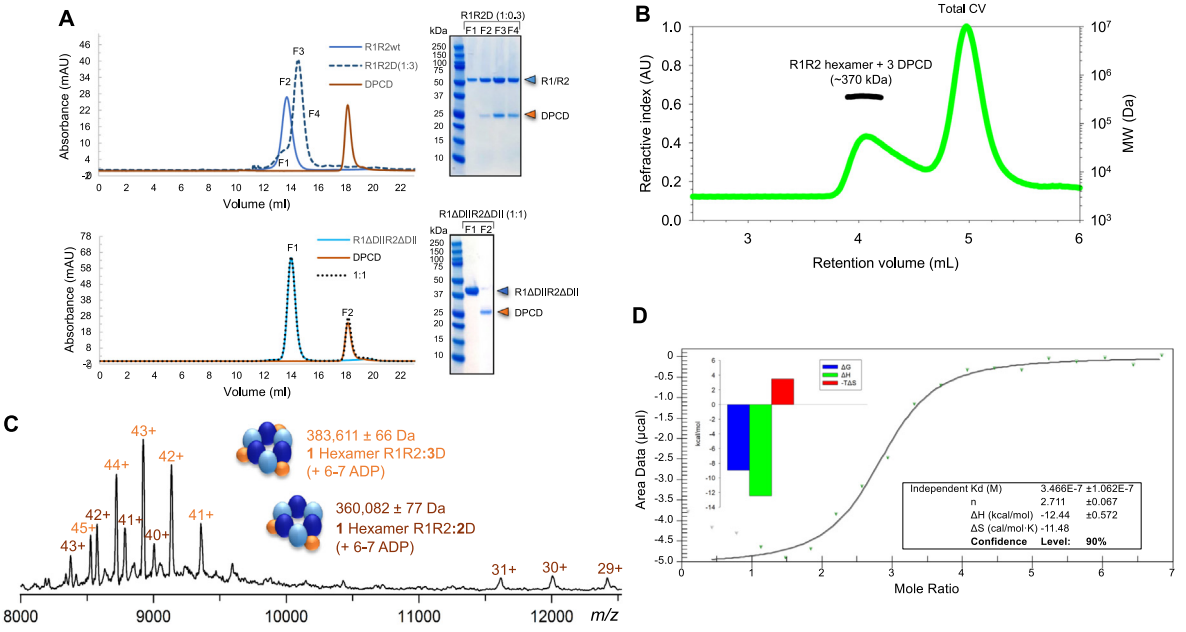

Figure 3. DPCD interacts directly with R1/R2. (**A**) Chromatographic co-elution assay followed by SDS-PAGE analysis. (**B**) SEC-SLS analysis highlighting a 3:3:3 stoichiometry of the R1R2D complex. CV and MW are the column volume and the molecular weight, respectively. (**C**) High resolution native MS analysis confirming the stoichiometry, i.e., 3 DPCD per 1 R1/R2 hexamer. (**D**) ITC analysis of the interaction. Dissociation constant (K_d), stoichiometry (n), variation in enthalpy (ΔH), in entropy (ΔS), and in free energy (ΔG) are reported along with the thermodynamic signature.

The assembly of the R1R2D complex was also assessed by DSF (Figure S6) to evaluate how complex association influences overall thermostability and how DPCD modulates the R1R2 ring oligomeric state *in-vitro*. R1R2 presents two thermal melting transitions (*Tm*), 48 °C and 54 °C (Figures S6(A and C)) that were tentatively assigned to the DII domains and the core ring region, respectively. This assignment is supported by the single melting transition observed for the R1R2_ΔDII complex, with a *Tm* of 53 °C (Figures S6(B and C)). DPCD alone presented a single melting transition at 55 °C, while the R1R2D complex showed a *Tm* value at 50 °C, suggesting complex formation via DII, thus stabilizing the lower observed *Tm* component assigned to DII. Conversely, no similar effect was observed for R1R2_ΔDII (DII_truncated) when incubated with DPCD (Figures S6(B and C)), as no interaction was expected. The emerging R1R2D hexameric complex may also justify overall lower thermostability compared to the R1R2 dodecamer.

Altogether, these complementary and orthogonal biophysical techniques allowed us to unambiguously demonstrate that DPCD binds to DII domains of R1 and R2 with a K_d in the sub-micromolar range and displaces the R1R2 dodecameric/hexameric equilibrium towards a stable R1R2D complex consisting of three DPCD per one R1R2 hexamer.

Topological investigation of the interaction between R1R2 and DPCD

First, SEC-SAXS experiments were performed on the R1R2D complex (Figures 4(A–D) and Tables S2 and S3). Remarkably, the R1R2D complex harbored a constant R_g in a R_g versus a frame number plot, attesting to the homogeneity and the stability of the complex even after several dilution/concentration steps (Figure 4(A)). The scattering curve of the R1R2D complex is shown in Figure 4(B). The R_g value determined for R1R2D was 54 Å (Table S3). In comparison, a R_g value of ∼ 52 Å was determined for a pure R2 hexamer.[20] The same theoretical R_g value of ∼ 52 Å was obtained for R1R2 hexamers both having DII up conformation (DII_{ext} stretched upward in the direction of the solvent, PDB: 7OLE). On the other hand, a theoretical R_g value of ∼ 45 Å was determined for hexameric R1R2 with DII down conformation (DII_{ext} stretched downward), in the context of INO80 (PDB: 5OAF). The R_g value of R1R2D (54 Å) could be due to DII conformation and/or DPCD contribution which might be buried in DII domains or exposed to the solvent. The P(r) profiles reached maximum around 60 Å and a *Dmax* of 159 Å (Figure 4(C)) in line with the dimension of DPCD with hexameric R1R2 and not with dodecameric R1R2. On dimensionless Kratky-plots (Figure 4(D))[54] the maximum observed at ∼ 1.1 for a

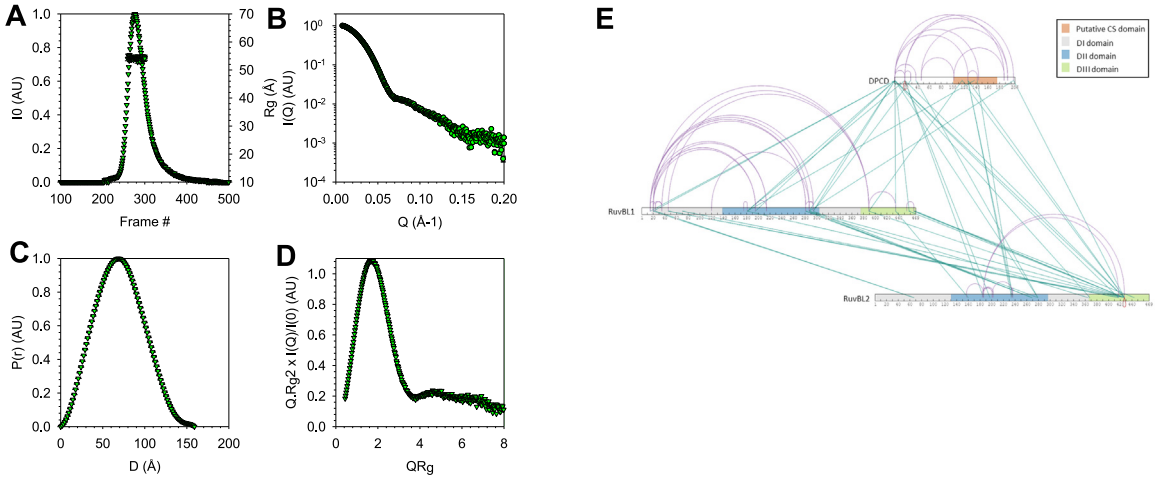

Figure 4. Comparative analysis by SAXS and XL-MS. (**A**) SEC-SAXS profile. I(0) and *Rg* of different fractions measured across the single SEC peak. (**B**) Scattering intensity I(q) vs Q plot. (**C**) Pair distribution function analysis. (**D**) Dimensionless Kratky plots. R1R2 are in red and R1R2D in green. (**E**) XL-MS map (inter-links in green, intra-links in magenta).

QR_g value of 1.7 ($\sqrt{3}$) is typical of globular proteins, while higher QR_g values suggest the presence of flexible domains.

To use an orthogonal method to SEC-SAXS, we performed IM-MS measurements on R1R2 hexamers (Figure S5) and R1R2D under native conditions, which yielded collision cross section ($^{TW}CCS_{N2}$) values of 13,081 ± 10 Å^2 and 15,225 ± 34 Å^2 for hexameric R1R2 (36 + charge state) and R1R2D (41 + charge state), respectively (Table S2). This ∼ 16% increase in $^{TW}CCS_{N2}$ upon DPCD binding to hexameric R1R2 agrees with both mass-based CCS estimations (∼ 15%) and in-solution SAXS data (∼ 20%). In addition, when $^{TW}CCS_{N2}$ was converted into an experimental $R_{IM\text{-}MS}$ radius for globular proteins, a value of 70 ± 3 Å was obtained for the R1R2D complex, in agreement with R_h = 73 Å as determined with SEC (Table S2), showing that the native global conformation of R1R2D is preserved in the gas phase. Taken together, the SEC-SAXS and IM-MS experiments support the hypothesis that the global shape of the hexameric R1R2 is maintained upon DPCD binding.

Knowing that the interaction occurs mainly via the DII domain, we next mapped which region of DPCD interacts with R1R2 using XL-MS experiments with DSBU, which reacts specifically with Lys residues, as chemical reagent (Figure 4(E)). To evaluate the reliability of our XL-MS experiments, we first compared R1R2 inter- and intra-cross-links on available R1R2 cryo-EM structures either in DII up (PDB: 7OLE) or DII down conformation (PDB: 5OAF). Considering a constraint distance cut-off of 6 to 30 Å, more cross-linked peptides (both intra and inter) were validated for the DII down stretched structure (23/32 XL peptides, 72% for 5OAF compared to 20/31, 65% for 7OLE), suggesting that DPCD rather binds to R1R2 in its DII down conformation. Concerning the R1R2D complex, 13 inter-cross-links (8 involving DPCD N-ter) were identified between DPCD and R1, while 14 cross-links (4 involving DPCD N-ter) were identified with R2. Interestingly, the inter-R1R2-DPCD cross-links identified included three different DPCD regions (Figure 4(E)): one at the N-terminus, another at the C-terminus parts corresponding to predicted α-helices located close together, the last region in the putative predicted CS domain. On R1 or R2 sides, DPCD cross-links were identified mainly in the DII domain (8/13 and 7/14 for R1 and R2, respectively) as expected (Figure 4(E)). Interestingly, comparison of intra cross-linked peptides for DPCD alone or in complex with R1R2 revealed mostly similar residues involved. However, two additional regions involving K46 and K102 were detected in R1R2D complex, suggesting conformational rearrangements within DPCD upon R1R2D complex formation (Figure S7).

Finally, negative staining transmission electron microscopy assays, followed by 2D classifications of the different observed complexes were conducted. Comparative observations of R1R2 (Figures 5(A–D) and S8, respectively with and without their DII domains) and *in vitro* reconstituted R1R2D complexes (Figures 5(C–D)) revealed clear morphological differences between R1R2 and R1R2D complexes. Most R1R2 particles (80% of the analyzed population) appeared to be rectangular, and their shape and dimensions (∼ 13 × 11 nm) corresponded to side views of dodecameric assemblies, made of two rings of hexamers (Figure 5(B)). The remaining 20% of the analyzed particles was grouped into 2D classes with round/hexameric shapes, of

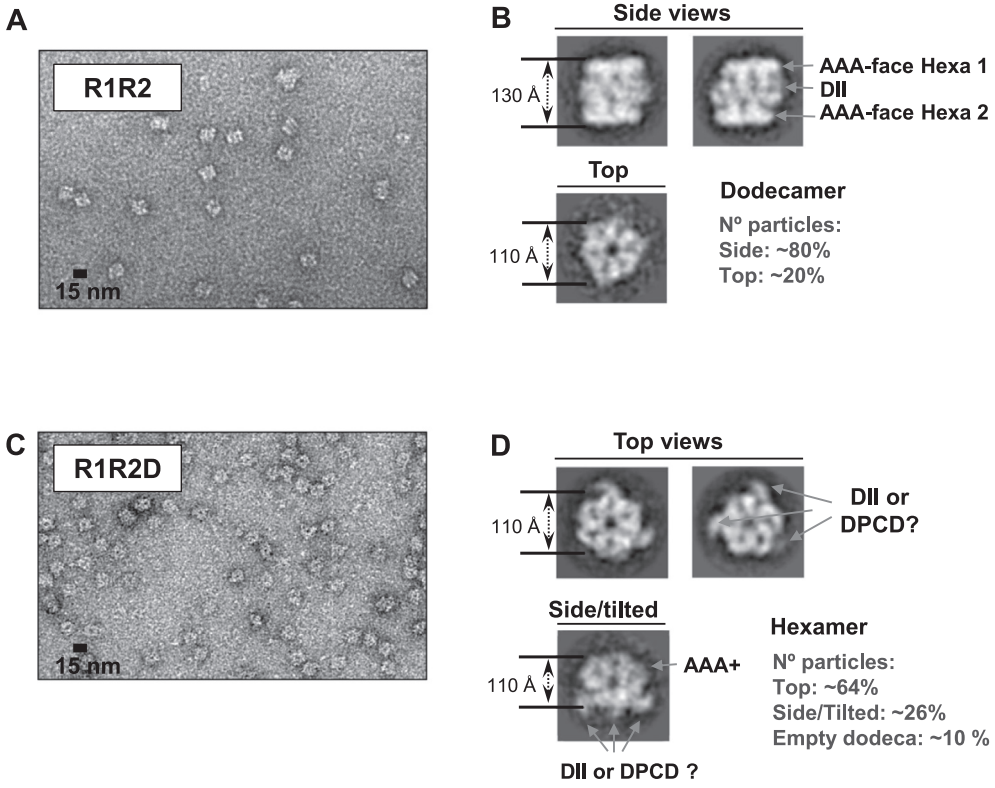

Figure 5. Overall structure of the R1R2D complex. Negative stain electron microscopy images of R1R2 (**A**) and R1R2D (**C**). Typical 2D class sums of R1R2 (**B**) and R1R2D (**D**) obtained after single particle analysis. The distribution of the analyzed particles according to their orientation (top, side, or tilted views) is indicated in the lower right panel.

11 nm in diameter, which were attributed to top views of this assembly (i.e., views of the hexameric rings of the dodecamers, along their 6-fold symmetry axis) (Figure 5(B) and S8). Similar observations were made for R1ΔDII/R2ΔDII particles, clearly harboring double-ringed side views typical of dodecameric assemblies (Figure S8). However, R1ΔDII/R2ΔDII particles seem to adopt a more rectangular shape than their full-length counterpart, which resembles more a parallelogram, suggesting a skewed piling of the two hexameric rings for the full-length R1R2 particles. In contrast, most R1R2D complexes (64%) appeared to be round/hexameric in shape, with a diameter of ∼ 11 nm, which would be in good agreement with hexamers seen from the top. The presence of three prominences outside the round could correspond to the DIIs or DPCDs. Other views, representing 26% of the observed R1R2D complexes, were attributed to side or tilted views of single-ringed hexamers, while only 10% seem to correspond to side views of double-ringed hexamers, thus dodecameric assemblies. These observations strongly suggest that DPCD association to R1/R2 disrupts its dodecameric assembly.

Discussion

To date, although DPCD has appeared in several proteomic analyses, very little is known about its function. In this study, we have characterized the DPCD protein at the cellular, biochemical, molecular and topological level. DPCD associates with R1R2 *in vivo* to form a specific and strong R1R2D complex. It also associates with other R2TP/R2TP-like/PAQosome components or cofactors like RPAP3, PIH1D1, WDR92, POLR2E, ZNHIT2, and EFTUD2. According to the predicted 3D structure, DPCD is a monomeric protein likely comprising one β-sheet at the N-terminus, a flexible internal linker region, followed by a well-folded CS domain at the C-terminus, and finally-two additional N- and C-ter α-helices. The direct interaction between DPCD and the R1R2 complex was evidenced and thoroughly investigated using a combination of biophysical and structural techniques. *In vitro*, the R1R2 complex includes up to 3 DPCD molecules in direct interaction with R1R2 in a hexameric ring (Figure 3(C)). The specific and high-affinity (sub-micromolar range) interaction with the R1R2 ring establishes it as a new AAA + ATPase cofactor. The interaction

occurs mainly via the DII domains of two consecutive R1R2 within hexameric state and through three distant regions on DPCD monomer, including the N-terminal helix, the putative CS domain but also the region at the C-terminal extremity. Finally, the negative stain electron microscopy images of R1R2D (Figure 5(D)) indicate the presence of three protuberances on the lower outer side of the DII-face of hexameric R1R2 which may correspond either to the DII_{ext} of 3R1 or 3R2 in up conformation or to the three molecules of DPCD.

The oligomeric state of R1(Rvb1)R2(Rvb2) in bound form is hexameric with the DII-face as a scaffold platform with the exception of INO80 Chromatin Remodeling Complexes for which are still being debated.[55–57] It has been proposed that the dodecameric form of R1R2 functions as a storage form.[18,58] In solution, the R1R2 complex alone with the RUVBL1 protomers N-terminally tagged, is predominantly dodecameric (Figures 3(A), 5(A–B), and S5). We used this oligomeric state as a tool to clearly demonstrate the formation of a complex between the R1R2 complex and DPCD. This observation showed that DPCD alters the dodecameric state of R1R2 *in vitro*, by interacting predominantly with the DIIs. This interaction also raises the question of whether DPCD can regulate the RUVBL's ATPase activity cycle. Using LUMIER-IP, we confirmed the strong interaction of DPCD with R1 WT and R2 WT but we detected no interaction with the $R1^{E303Q}$ mutant form (weak for $R2^{E300Q}$). The ATP-hydrolysis deficient $R1^{E303Q}R2^{E300Q}$ exhibited similar oligomerization to the wild-type complex,[23] which excludes the change in oligomerization of R1R2 as a driver of the absence of interaction in cells. Freezing of the ATP bound molecule in the nucleotide pocket by the mutants (inactive ATP state) seems to negatively affect the affinity between DPCD and the R1R2 complex. On the other hand, ADP had no effect on the interaction between R1R2 and DPCD *in vitro* and probably not *in vivo*. Despite the absence of ADP molecules in our RUVBL purification and analysis buffers, our native MS analysis showed trapping of 6 ADP molecules per hexamer. These nucleotides probably originate from *E. coli*. The interaction between R1R2 and DPCD therefore takes place in the presence of ADP *in vitro* (Figure 3(C)). As the number of ADP molecules in R1R2 did not change during the interaction, DPCD may drive the switch from dodecameric to hexameric forms of R1R2. From a mechanistic point of view, any factor that influences this dodecamer/hexamer transition is essential because this transition is the basis of the core activity of RUVBLs/Rvbs, associated with their chaperone function.[59]

The influence of ATP on the R1R2 active site has previously been reported to affect partner binding. R1 and R2 associate with partners of the PAQosome assembly pathways as well as some PAQosome substrates more efficiently in presence of one selective ATPase inhibitor, the compound B.[16] This molecule, like its daughter, CB-6644, binds and stabilizes only the ATP-bound state of hetero-assembled R1R2.[32] ATP hydrolysis could serve to mature the client or/and disengage hetero-hexameric R1R2 from its partners and clients. In cells, we showed that DPCD does not associate with the R1R2 in the presence of the CB-6644 inhibitor. We hypothesize that the *in vivo* ATP-bound R1R2 WT may become activated in a conformation where different partner proteins preferentially associate with R1R2, thus preventing or limiting DPCD binding.

After R1R2, our GFP:DPCD SILAC-IP results showed two enriched partners (Figure 1(B)), the components of human PAQosome, WDR92 and RPAP3. LUMIER-IP also revealed a strong association, suggesting direct *in cellulo* interaction between WDR92 and the N-terminal region of RPAP3 (Figure 1(D)). The association loss observed for full-size RPAP3 could be explained by the inaccessibility of its N-terminal part via homo-dimerization. Our finding confirms and refines, at the domain level, recent reports in *Drosophila* and *Chlamydomonas*.[58,31] For years, it has been reported that human WDR92 associates with the TPR or C-ter domains of RPAP3.[61] These domains allow the recruitment of chaperones HSP70/90 and RUVBLs, respectively. As an example, SILAC-IP experiments in HEK293T with GFP:RPAP3-Cter as bait did not show WDR92 to be the enriched partner but rather first, R1R2 and second, DPCD.[11] Human WDR92 and Wdr92 in *Drosophila* associate respectively with SPAG1, a paralog of RPAP3 in human and Spag1, a paralog of Spaghetti (Spag) in *Drosophila*.[8,31] Like RPAP3 protein, human SPAG1 includes several TPRs and a RPAP3-C domains but *Drosophila* Spag1 only comprises a N-terminal region with a single TPR domain. Our demonstration of the RPAP3 N-terminal region as a WDR92 recognition site instead of its TPR or C-terminal domains explains why *Drosophila* Spag1 conserves the dynein assembly function of human SPAG1 proteins in Zur Lage's results.

The direct interaction between DPCD and R1R2 has just been assessed, but the DPCD behavior towards other R2TP or R2TP-like components remained to be elucidated. Notably, DPCD is expressed in ciliated cells, particularly in testis,[7–8] like R2SP, which is also enriched in testis.[11] AP-MS analysis of *Drosophila* testis revealed association between Wdr92 and the prefoldin subunits, both dynein HCs and ICs, Spag, Spag1 and Dnaaf1.[31] Wdr92 interacts directly with both dynein HCs and ICs. It is tempting to speculate that DPCD, SPAG1 and WDR92 are involved in regulating dynein assembly in the testis. It raises the question of whether DPCD could be a specific adapter of R2SP, a R2TP/PAQosome client, or an exclusive

partner of R1R2. Perhaps new DPCD partners still need to be identified to better understand its biological function. To this end, working with other cellular models is probably necessary. Use ciliated or testicular cells appear to be essential to fully decipher DPCD cellular function.

This study unveiled important functional and molecular determinants suggesting DPCD as a novel direct interactor of the R1R2 that regulate the oligomerization state of R1R2 complex and raises new questions about the regulatory mechanism of the ATPase activity cycle of the RUVBLs that is essential for cell metabolism. A high-resolution structural study by cryo-EM of the R1R2D complex would pave the way for more in-depth of interacting regions. The role of the R1R2D complex in primary ciliary dyskinesia should be elucidated in future research.

Data Availability

The NMR chemical shift have been deposited in the BMRB - Biological Magnetic Resonance Bank with entry 51533.

DECLARATION OF COMPETING INTEREST

The authors declare that they have no known competing financial interests or personal relationships that could have appeared to influence the work reported in this paper.

Acknowledgments

The authors would like to thank S. Balor and V. Soldan (METI platform, Toulouse), for technical support in electron microscopy. The negative stain EM image analysis was performed using High Performance Computing resources from CALMIP (grant 2020-P1406). We thank the Biophysics and Structural Biology (B2S) platform of IBSLor (UMS 2008/US 40) for access to the NMR, ITC, CD, and SLS core facilities (https://umsibslor.univ-lorraine.fr/en/facility/biophysics-structural-biology-b2s). We also thank the Functional Proteomic Platform of Montpellier (FFP). Financial support from the IR-RMN-THC FR3050 CNRS for conducting the research is gratefully acknowledged. We also thank Javiez Perez and Aurélien Thureau for assistance with the SWING beamline. SOLEIL Synchrotron is acknowledged for providing beamtime and synchrotron radiation facilities. This work was supported by the French *Centre National de la Recherche Scientifique* (CNRS), Université de Lorraine (UL), Université de Strasbourg (Unistra), the *Agence Nationale de la Recherche* [ANR-16-CE11-0032-04], the *Ligue Nationale Contre le Cancer ('équipe labellisée')*, *Institut national du Cancer* [INCa PLBio 2016-161], and the French Proteomics Infrastructure (ProFI; ANR-10-INBS-08-03). The authors would like to thank GIS IBiSA and *Région Alsace* for financial support in purchasing a Synapt G2 HDMS and Orbitrap Exactive Plus EMR instrument, respectively. E.D. acknowledges the French Ministry for Education and Research for funding of her PhD fellowship. M.L was granted by the ANR and S.H. by UCB. R.D.S.M. received young researcher funding from the *région Grand-Est*. Y.A. was supported by INCa and ANR. iNOVA4Health – UIDB/04462/2020 and UIDP/04462/2020, a program financially supported by *Fundação para a Ciência e Tecnologia / Ministério da Ciência, Tecnologia e Ensino Superior,* Portugal, through national funds is acknowledged.

Appendix A. Supplementary data

Supplementary data to this article can be found online at https://doi.org/10.1016/j.jmb.2022.167760.

Received 4 February 2022;
Accepted 21 July 2022;
Available online 25 July 2022

Keywords:
DPCD;
RUVBL1;
RUVBL2;
SILAC-IP;
LUMIER-IP;
SAXS;
structural MS;
EM

† Authors contributed equally.

References

1. Kobayashi, Y., Watanabe, M., Okada, Y., Sawa, H., Takai, H., Nakanishi, M., Kawase, Y., Suzuki, H., et al., (2002). Hydrocephalus, Situs Inversus, Chronic Sinusitis, and Male Infertility in DNA Polymerase λ-Deficient Mice: Possible Implication for the Pathogenesis of Immotile Cilia Syndrome. *Mol. Cell. Biol.* **22**, 2769–2776. https://doi.org/10.1128/MCB.22.8.2769-2776.2002.
2. King, S.M., Sale, W.S., (2018). Fifty years of microtubule sliding in cilia. *Mol. Biol. Cell* **29**, 698–701. https://doi.org/10.1091/mbc.E17-07-0483.
3. King, S.M., (2018). Dyneins: Structure, Biology and Disease. Elsevier: Academic Press, Oxford, UK.
4. Oda, T., Yanagisawa, H., Kamiya, R., Kikkawa, M., (2014). A molecular ruler determines the repeat length in eukaryotic cilia and flagella. *Science* **346**, 857–860. https://doi.org/10.1126/science.1260214.
5. Knowles, M.R., Daniels, L.A., Davis, S.D., Zariwala, M.A., Leigh, M.W., (2013). Primary Ciliary Dyskinesia. Recent Advances in Diagnostics, Genetics, and Characterization of Clinical Disease. *Am. J. Respir. Crit. Care Med.* **188**, 913–922. https://doi.org/10.1164/rccm.201301-0059CI.
6. Vogel, P., Read, R., Hansen, G.M., Freay, L.C., Zambrowicz, B.P., Sands, A.T., (2010). Situs inversus in

Dpcd/Poll-/-, Nme7-/-, and Pkd1l1-/- mice. *Vet. Pathol.* **47**, 120–131. https://doi.org/10.1177/0300985809353553.
7. Zariwala, M., O'Neal, W.K., Noone, P.G., Leigh, M.W., Knowles, M.R., Ostrowski, L.E., (2004). Investigation of the possible role of a novel gene, DPCD, in primary ciliary dyskinesia. *Am. J. Respir. Cell Mol. Biol.* **30**, 428–434. https://doi.org/10.1165/rcmb.2003-0338RC.
8. Li, S., Ao, L., Yan, Y., Jiang, J., Chen, B., Duan, Y., Shen, F., Chen, J., et al., (2019). Differential motility parameters and identification of proteomic profiles of human sperm cryopreserved with cryostraw and cryovial. *Clin. Proteomics* **16**, 24. https://doi.org/10.1186/s12014-019-9244-2.
9. Cloutier, P., Poitras, C., Durand, M., Hekmat, O., Fiola-Masson, É., Bouchard, A., Faubert, D., Chabot, B., et al., (2017). R2TP/Prefoldin-like component RUVBL1/RUVBL2 directly interacts with ZNHIT2 to regulate assembly of U5 small nuclear ribonucleoprotein. *NatureCommun* **8**, 15615. https://doi.org/10.1038/ncomms15615.
10. Huttlin, E.L., Bruckner, R.J., Paulo, J.A., Cannon, J.R., Ting, L., Baltier, K., Colby, G., Gebreab, F., et al., (2017). Architecture of the human interactome defines protein communities and disease networks. *Nature* **545**, 505–509. https://doi.org/10.1038/nature22366.
11. Maurizy, C., Quinternet, M., Abel, Y., Verheggen, C., Santo, P.E., Bourguet, M., Paiva, C.F., A., Bragantini, B., Chagot, M.-E., Robert, M.-C.,, (2018). The RPAP3-Cterminal domain identifies R2TP-like quaternary chaperones. *Nature Commun.* **9** https://doi.org/10.1038/s41467-018-04431-1.
12. Rolland, T., Taşan, M., Charloteaux, B., Pevzner, S.J., Zhong, Q., Sahni, N., Yi, S., Lemmens, I., et al., (2014). A proteome-scale map of the human interactome network. *Cell* **159**, 1212–1226. https://doi.org/10.1016/j.cell.2014.10.050.
13. Dafinger, C., Rinschen, M.M., Borgal, L., Ehrenberg, C., Basten, S.G., Franke, M., Höhne, M., Rauh, M., et al., (2018). Targeted deletion of the AAA-ATPase Ruvbl1 in mice disrupts ciliary integrity and causes renal disease and hydrocephalus. *Exp. Mol. Med.* **50**, 75. https://doi.org/10.1038/s12276-018-0108-z.
14. Mitchell, D.R., (2018). Cytoplasmic preassembly and trafficking of axonemal dyneins. *In: Dyneins: Structure, Biology and Disease*. Elsevier: Academic Press), (Oxford, UK, pp. 141–161.
15. Zhao, R., Davey, M., Hsu, Y.-C., Kaplanek, P., Tong, A., Parsons, A.B., Krogan, N., Cagney, G., et al., (2005). Navigating the Chaperone Network: An Integrative Map of Physical and Genetic Interactions Mediated by the Hsp90 Chaperone. *Cell* **120**, 715–727. https://doi.org/10.1016/j.cell.2004.12.024.
16. Yenerall, P., Das, A.K., Wang, S., Kollipara, R.K., Li, L.S., Villalobos, P., Flaming, J., Lin, Y.-F., et al., (2020). RUVBL1/RUVBL2 ATPase Activity Drives PAQosome Maturation, DNA Replication and Radioresistance in Lung Cancer. *Cell Chemical Biology* **27**, 105–121.e14. https://doi.org/10.1016/j.chembiol.2019.12.005.
17. Gorynia, S., Bandeiras, T.M., Pinho, F.G., McVey, C.E., Vonrhein, C., Round, A., Svergun, D.I., Donner, P., et al., (2011). Structural and functional insights into a dodecameric molecular machine – The RuvBL1/RuvBL2 complex. *J. Struct. Biol.* **176**, 279–291. https://doi.org/10.1016/j.jsb.2011.09.001.
18. Lakomek, K., Stoehr, G., Tosi, A., Schmailzl, M., Hopfner, K.P., (2015). Structural basis for dodecameric assembly states and conformational plasticity of the full-length AAA+ ATPases Rvb1. Rvb2. *Structure* **23**, 483–495. https://doi.org/10.1016/j.str.2014.12.015.
19. Matias, P.M., Gorynia, S., Donner, P., Carrondo, M.A., (2006). Crystal structure of the human AAA+ protein RuvBL1. *J. Biol. Chem.* **281**, 38918–38929. https://doi.org/10.1074/jbc.M605625200.
20. Silva, S.T.N., Brito, J.A., Arranz, R., Sorzano, C.Ó.S., Ebel, C., Doutch, J., Tully, M.D., Carazo, J.-M., et al., (2018). X-ray structure of full-length human RuvB-Like 2 – mechanistic insights into coupling between ATP binding and mechanical action. *Sci. Rep.* **8**, 13726. https://doi.org/10.1038/s41598-018-31997-z.
21. Martino, F., Pal, M., Muñoz-Hernández, H., Rodríguez, C. F., Núñez-Ramírez, R., Gil-Carton, D., Degliesposti, G., Skehel, J.M., et al., (2018). RPAP3 provides a flexible scaffold for coupling HSP90 to the human R2TP co-chaperone complex. *Nature Commun.* **9**, 1501. https://doi.org/10.1038/s41467-018-03942-1.
22. Muñoz-Hernández, H., Pal, M., Rodríguez, C.F., Fernandez-Leiro, R., Prodromou, C., Pearl, L.H., Llorca, O., (2019). Structural mechanism for regulation of the AAA-ATPases RUVBL1-RUVBL2 in the R2TP co-chaperone revealed by cryo-EM. Science. *Advances* **5**, eaaw1616. https://doi.org/10.1126/sciadv.aaw1616.
23. López-Perrote, A., Hug, N., González-Corpas, A., Rodríguez, C.F., Serna, M., García-Martín, C., Boskovic, J., Fernandez-Leiro, R., et al., (2020). Regulation of RUVBL1-RUVBL2 AAA-ATPases by the nonsense-mediated mRNA decay factor DHX34, as evidenced by Cryo-EM. *ELife* **9**, e63042.
24. Serna, M., González-Corpas, A., Cabezudo, S., López-Perrote, A., Degliesposti, G., Zarzuela, E., Skehel, J.M., Muñoz, J., Llorca, O., (2021). CryoEM of RUVBL1–RUVBL2–ZNHIT2, a complex that interacts with pre-mRNA-processing-splicing factor 8. *Acids Res. Nucl.*. https://doi.org/10.1093/nar/gkab1267.
25. Seraphim, T.V., Nano, N., Cheung, Y.W.S., Aluksanasuwan, S., Colleti, C., Mao, Y.-Q., Bhandari, V., Young, G., et al., (2021). Assembly principles of the human R2TP chaperone complex reveal the presence of R2T and R2P complexes. *Structure*. https://doi.org/10.1016/j.str.2021.08.002.
26. Coulombe, B., Cloutier, P., Gauthier, M.-S., (2018). How do our cells build their protein interactome? *Nature Commun.* **9**, 2955. https://doi.org/10.1038/s41467-018-05448-2.
27. Houry, W.A., Bertrand, E., Coulombe, B., (2018). The PAQosome, an R2TP-Based Chaperone for Quaternary Structure Formation. *Trends Biochem. Sci.* **43**, 4–9. https://doi.org/10.1016/j.tibs.2017.11.001.
28. Cloutier, P., Poitras, C., Faubert, D., Bouchard, A., Blanchette, M., Gauthier, M.-S., Coulombe, B., (2020). Upstream ORF-Encoded ASDURF Is a Novel Prefoldin-like Subunit of the PAQosome. *J. Proteome Res.* **19**, 18–27. https://doi.org/10.1021/acs.jproteome.9b00599.
29. Patel-King, R.S., Sakato-Antoku, M., Yankova, M., King, S. M., (2019). WDR92 is required for axonemal dynein heavy chain stability in cytoplasm. *MBoC* **30**, 1834–1845. https://doi.org/10.1091/mbc.E19-03-0139.
30. Leader, D.P., Krause, S.A., Pandit, A., Davies, S.A., Dow, J.A.T., (2018). FlyAtlas 2: a new version of the Drosophila melanogaster expression atlas with RNA-Seq, miRNA-Seq

and sex-specific data. *Nucleic Acids Res.* **46**, D809–D815. https://doi.org/10.1093/nar/gkx976.
31. Zur Lage, P., Stefanopoulou, P., Styczynska-Soczka, K., Quinn, N., Mali, G., von Kriegsheim, A., Mill, P., Jarman, A. P., (2018). Ciliary dynein motor preassembly is regulated by Wdr92 in association with HSP90 co-chaperone, R2TP. *The Journal of Cell Biology* **217**, 2583–2598. https://doi.org/10.1083/jcb.201709026.
32. Assimon, V.A., Tang, Y., Vargas, J.D., Lee, G.J., Wu, Z.Y., Lou, K., Yao, B., Menon, M.-K., et al., (2019). CB-6644 Is a Selective Inhibitor of the RUVBL1/2 Complex with Anticancer Activity. *ACS Chem. Biol.* **14**, 236–244. https://doi.org/10.1021/acschembio.8b00904.
33. Diebold, M.L., Fribourg, S., Koch, M., Metzger, T., Romier, C., (2011). Deciphering correct strategies for multiprotein complex assembly by co-expression: Application to complexes as large as the histone octamer. *J. Struct. Biol.*. https://doi.org/10.1016/j.jsb.2011.02.001.
34. Micsonai, A., Wien, F., Kernya, L., Lee, Y.-H., Goto, Y., Réfrégiers, M., Kardos, J., (2015). Accurate secondary structure prediction and fold recognition for circular dichroism spectroscopy. *PNAS* **112**, E3095–E3103. https://doi.org/10.1073/pnas.1500851112.
35. Micsonai, A., Wien, F., Bulyáki, É., Kun, J., Moussong, É., Lee, Y.-H., Goto, Y., Réfrégiers, M., et al., (2018). BeStSel: a web server for accurate protein secondary structure prediction and fold recognition from the circular dichroism spectra. *Nucleic Acids Res.* **46**, W315–W322. https://doi.org/10.1093/nar/gky497.
36. Keller, R.L.J., (2004). Computer-Aided Resonance Assignment Tutorial. CANTINA Verlag, Zürich.
37. Shen, Y., Bax, A., (2013). Protein backbone and sidechain torsion angles predicted from NMR chemical shifts using artificial neural networks. *J. Biomol. NMR* **56**, 227–241. https://doi.org/10.1007/s10858-013-9741-y.
38. Keller, S., Vargas, C., Zhao, H., Piszczek, G., Brautigam, C.A., Schuck, P., (2012). High-Precision Isothermal Titration Calorimetry with Automated Peak-Shape Analysis. *Anal. Chem.* **84**, 5066–5073. https://doi.org/10.1021/ac3007522.
39. Bush, M.F., Hall, Z., Giles, K., Hoyes, J., Robinson, C.V., Ruotolo, B.T., (2010). Collision Cross Sections of Proteins and Their Complexes: A Calibration Framework and Database for Gas-Phase Structural Biology. *Anal. Chem.* **82**, 9557–9565. https://doi.org/10.1021/ac1022953.
40. Ruotolo, B.T., Benesch, J.L.P., Sandercock, A.M., Hyung, S.-J., Robinson, C.V., (2008). Ion mobility–mass spectrometry analysis of large protein complexes. *Nature Protoc.* **3**, 1139–1152. https://doi.org/10.1038/nprot.2008.78.
41. Shrivastav, V., Nahin, M., Hogan, C.J., Larriba-Andaluz, C., (2017). Benchmark Comparison for a Multi-Processing Ion Mobility Calculator in the Free Molecular Regime. *J. Am. Soc. Mass Spectrom.* **28**, 1540–1551. https://doi.org/10.1021/jasms.8b05613.
42. Atmanene, C., Chaix, D., Bessin, Y., Declerck, N., Van Dorsselaer, A., Sanglier-Cianferani, S., (2010). Combination of Noncovalent Mass Spectrometry and Traveling Wave Ion Mobility Spectrometry Reveals Sugar-Induced Conformational Changes of Central Glycolytic Genes Repressor/DNA Complex. *Anal. Chem.* **82**, 3597–3605. https://doi.org/10.1021/ac902784n.
43. Franke, D., Petoukhov, M.V., Konarev, P.V., Panjkovich, A., Tuukkanen, A., Mertens, H.D.T., Kikhney, A.G., Hajizadeh, et al., (2017). ATSAS 2.8: a comprehensive data analysis suite for small-angle scattering from macromolecular solutions. *J Appl Cryst* **50**, 1212–1225. https://doi.org/10.1107/S1600576717007786.
44. Rambo, R.P., Tainer, J.A., (2013). Accurate assessment of mass, models and resolution by small-angle scattering. *Nature* **496**, 477–481. https://doi.org/10.1038/nature12070.
45. Yang, J., Anishchenko, I., Park, H., Peng, Z., Ovchinnikov, S., Baker, D., (2020). Improved protein structure prediction using predicted interresidue orientations. *PNAS* **117**, 1496–1503. https://doi.org/10.1073/pnas.1914677117.
46. Baek, M., DiMaio, F., Anishchenko, I., Dauparas, J., Ovchinnikov, S., Lee, G.R., Wang, J., Cong, Q., et al., (2021). Accurate prediction of protein structures and interactions using a three-track neural network. *Science* **373**, 871–876. https://doi.org/10.1126/science.abj8754.
47. Jumper, J., Evans, R., Pritzel, A., Green, T., Figurnov, M., Ronneberger, O., Tunyasuvunakool, K., Bates, R., et al., (2021). Highly accurate protein structure prediction with AlphaFold. *Nature* **596**, 583–589. https://doi.org/10.1038/s41586-021-03819-2.
48. Panjkovich, A., Svergun, D.I., (2016). Deciphering conformational transitions of proteins by small angle X-ray scattering and normal mode analysis. *PCCP* **18**, 5707–5719. https://doi.org/10.1039/C5CP04540A.
49. Valentini, E., Kikhney, A.G., Previtali, G., Jeffries, C.M., Svergun, D.I., (2015). SASBDB, a repository for biological small-angle scattering data. *Nucleic Acids Res.* **43**, D357–D363. https://doi.org/10.1093/nar/gku1047.
50. Zivanov, J., Nakane, T., Forsberg, B.O., Kimanius, D., Hagen, W.J., Lindahl, E., Scheres, S.H., (2018). New tools for automated high-resolution cryo-EM structure determination in RELION-3. *ELife* **7**, e42166.
51. Perez-Riverol, Y., Bai, J., Bandla, C., García-Seisdedos, D., Hewapathirana, S., Kamatchinathan, S., Kundu, D.J., Prakash, A., et al., (2022). The PRIDE database resources in 2022: a hub for mass spectrometry-based proteomics evidences. *Nucleic Acids Res.* **50**, D543–D552. https://doi.org/10.1093/nar/gkab1038.
52. Barrios-Rodiles, M., Brown, K.R., Ozdamar, B., Bose, R., Liu, Z., Donovan, R.S., Shinjo, F., Liu, Y., et al., (2005). High-throughput mapping of a dynamic signaling network in mammalian cells. *Science* **307**, 1621–1625. https://doi.org/10.1126/science.1105776.
53. Buchan, D.W.A., Jones, D.T., (2019). The PSIPRED Protein Analysis Workbench: 20 years on. *Nucleic Acids Res.* **47**, W402–W407. https://doi.org/10.1093/nar/gkz297.
54. Receveur-Brechot, V., Durand, D., (2012). How random are intrinsically disordered proteins? A small angle scattering perspective. *Curr. Protein Pept. Sci.* **13**, 55–75. https://doi.org/10.2174/138920312799277901.
55. Ayala, R., Willhoft, O., Aramayo, R.J., Wilkinson, M., McCormack, E.A., Ocloo, L., Wigley, D.B., Zhang, X., (2018). Structure and regulation of the human INO80–nucleosome complex. *Nature* **556**, 391–395. https://doi.org/10.1038/s41586-018-0021-6.
56. Eustermann, S., Schall, K., Kostrewa, D., Lakomek, K., Strauss, M., Moldt, M., Hopfner, K.-P., (2018). Structural basis for ATP-dependent chromatin remodelling by the INO80 complex. *Nature* **556**, 386–390. https://doi.org/10.1038/s41586-018-0029-y.
57. Tosi, A., Haas, C., Herzog, F., Gilmozzi, A., Berninghausen, O., Ungewickell, C., Gerhold, C.B., Lakomek, K., et al., (2013). Structure and subunit

topology of the INO80 chromatin remodeler and its nucleosome complex. *Cell* **154**, 1207–1219. https://doi.org/10.1016/j.cell.2013.08.016.

58. Silva-Martin, N., Dauden, M.I., Glatt, S., Hoffmann, N.A., Kastritis, P., Bork, P., Beck, M., Muller, C.W., (2016). The Combination of X-Ray Crystallography and Cryo-Electron Microscopy Provides Insight into the Overall Architecture of the Dodecameric Rvb1/Rvb2 Complex. *PLoS ONE* **11**, e0146457.
59. Zhou, C.Y., Stoddard, C.I., Johnston, J.B., Trnka, M.J., Echeverria, I., Palovcak, E., Sali, A., Burlingame, A.L., et al., (2017). Regulation of Rvb1/Rvb2 by a Domain within the INO80 Chromatin Remodeling Complex Implicates the Yeast Rvbs as Protein Assembly Chaperones. *Cell Reports* **19**, 2033–2044. https://doi.org/10.1016/j.celrep.2017.05.029.
60. Liu, G., Wang, L., Pan, J., (2018). Chlamydomonas WDR92 in association with R2TP-like complex and multiple DNAAFs to regulate ciliary dynein preassembly. *J. Mol. Cell. Biol.*. https://doi.org/10.1093/jmcb/mjy067.
61. Itsuki, Y., Saeki, M., Nakahara, H., Egusa, H., Irie, Y., Terao, Y., Kawabata, S., Yatani, H., et al., (2008). Molecular cloning of novel Monad binding protein containing tetratricopeptide repeat domains. *FEBS Letter* **582**, 2365–2370. https://doi.org/10.1016/j.febslet.2008.05.041.
62. Cox, J., Hein, M.Y., Luber, C.A., Paron, I., Nagaraj, N., Mann, M., (2014). Accurate proteome-wide label-free quantification by delayed normalization and maximal peptide ratio extraction, termed MaxLFQ. *Molecular & Cellular Proteomics : MCP* **13**, 2513–2526. https://doi.org/10.1074/mcp.M113.031591.